A Nature Portfolio journal



https://doi.org/10.1038/s42005-025-02292-x

# Generalized reciprocal diffractive imaging for reference-free, single-shot quantitative phase microscopy

Check for updates

Jeonghun Oh¹,², Herve Hugonnet ®¹,², Wei Sun Park ®¹,² & YongKeun Park ®¹,2,3 ⊠

Quantitative phase imaging (QPI) enables label-free measurement of intrinsic optical properties such as the refractive index, offering valuable insights into biological and medical samples. While reciprocal diffractive imaging (RDI) has demonstrated single-shot, reference-free reconstruction of complex optical fields from diffusive samples, its applicability to biological specimens has been limited due to dominant low-frequency components that hinder algorithmic convergence. Here, we present a generalized RDI method that overcomes this limitation by modulating the Fourier spectrum in the pupil plane using a custom-designed Fourier mask and a neutral density (ND) filter. This modification attenuates the DC term and enhances support boundary definition, enabling robust phase retrieval for non-diffusive samples. We validate the proposed method through both simulation and experiments, reconstructing known amplitude and phase objects as well as a range of biological samples including live cells and stained tissue sections. The approach is implemented in a conventional microscope without a reference arm, requiring only a simple pupil-plane modification. Our method provides a compact, non-interferometric solution for high-fidelity QPI and holds significant potential for broad applications in biomedical imaging and real-time dynamic studies.

Holography captures the full complex optical field—both amplitude and phase—thereby enabling precise reconstruction and manipulation of scattered light to visualize the object of interest¹. For thin and transparent samples, the phase component directly reflects intrinsic properties such as refractive index and sample thickness, making holography particularly valuable for quantitative phase imaging (QPI)². As a result, QPI has been widely applied in diverse biomedical fields, including histopathology³-6, microbiology³-9, hematology¹0-14, cell biology¹5-18, and preclinical study¹9-23. However, conventional holographic techniques typically rely on interferometric measurements with an external reference arm. This requirement increases the system complexity, introduces sensitivity to mechanical vibrations and environmental noise, and limits scalability due to bulky optical components. These limitations have motivated the development of reference-free alternatives that retain the phase retrieval capability of holography while simplifying the optical configuration.

The principle of non-interferometric holography fundamentally stands on the close relation between phase and intensity, which is represented by the Siegert relation<sup>24–26</sup>. The transport intensity equation (TIE)<sup>27,28</sup> is one of the non-interferometric techniques and deterministically derives the solution for the phase of light from two intensity

measurements: one in-plain and the other defocused. Differential phase microscopy  $(\mathrm{DPC})^{29,30}$  was proposed to retrieve quantitative wavefronts using two asymmetric illumination patterns. Fourier ptychographic microscopy  $(\mathrm{FPM})^{31,32}$  reconstructs the light field by iteratively filling the Fourier space from multiple intensity measurements from illumination under various angles. An analytical approach using the Kramers–Kronig  $(\mathrm{KK})$  relations suggested that under specific sample and illumination conditions, the real part of a complex light field determines the imaginary part, and vice versa, and unravels the intertwined relationship between phase and intensity.

Unfortunately, although the referred methods show promising capability in phase recovery and reveal intriguing physical implications, they have some limitations. The TIE does not provide a universal solution and needs approximations, such as the linear relationship between phase and intensity or strong assumptions for boundary conditions<sup>37</sup>. DPC linearizes the transmittance function of a sample, and KK holographic imaging derives holomorphic properties under the weak object approximation. FPM and KK holographic imaging demand multiple intensity maps to obtain a complete phase image, which hinders the observation of fast dynamics in biological objects. In addition, FPM has a heavy computational cost. It

<sup>&</sup>lt;sup>1</sup>Department of Physics, Korea Advanced Institute of Science and Technology (KAIST), Daejeon, Republic of Korea. <sup>2</sup>KAIST Institute for Health Science and Technology, Daejeon, Republic of Korea. <sup>3</sup>Tomocube, Inc. Daejeon, Republic of Korea. <sup>3</sup>Ee-mail: yk.park@kaist.ac.kr

should be noted that non-interferometric methods based on the synthetic aperture approach limit the imaging to thin samples.

Recently, reciprocal diffractive imaging (RDI)<sup>38</sup> has been proposed for imaging of diffusive objects via non-interferometric detection from a single-shot intensity image. RDI retrieves the complex optical field by reciprocally harnessing the reconstruction principle of coherent diffractive imaging. A Fourier mask that has an asymmetric shape at the pupil plane plays the role of the support in Fienup's hybrid input-output (HIO) algorithm<sup>39</sup>, and the constraints in Fourier and image spaces are iteratively applied to the output field in the previous step to reconstruct accurate scattered complex field. This approach provides a unique capability in retrieving diffusive fields, but the application to biological science and more general samples is restricted because the strong components around the DC term are problematic in meeting the condition that the support boundary should be clearly defined.

In this study, we present a generalized form of RDI that enables QPI of samples with dominant low-frequency (DC) components—such as biological cells and thin tissues—which are not compatible with the original RDI framework. To achieve this, we introduce a Fourier-plane modulation scheme using a custom-designed asymmetric mask combined with a neutral density (ND) filter, which attenuates the central spectrum and facilitates the definition of a well-bounded support. We validate the method through both simulation and experimental reconstruction of amplitude and phase objects, including biological cells and tissue sections. The results demonstrate that the proposed approach successfully extends RDI to a broader class of specimens while retaining a compact, reference-free optical setup. Owing to its simplicity, flexibility, and robustness, the generalized RDI method offers a powerful stand-alone solution for label-free, quantitative imaging across diverse biological applications.

## Results Principle

RDI exploits the HIO algorithm and is a reciprocal version of coherent diffractive imaging<sup>40-42</sup>, where the roles of the pupil and image plane are inverted. The measured intensity at the image plane and the known support at the pupil plane are used as constraints. A noncentrosymmetric Fourier mask located at the Fourier plane crops the Fourier field to make it asymmetric; this condition is required for the algorithm to lead to convergence to the correct solution<sup>39,43</sup>. If the Fourier mask is centrosymmetric, the iteration process fails, as shown in Fig. S1. When applying RDI to diffusive objects, the tight edge condition for the support can be easily met because the Fourier spectrum of the scattered

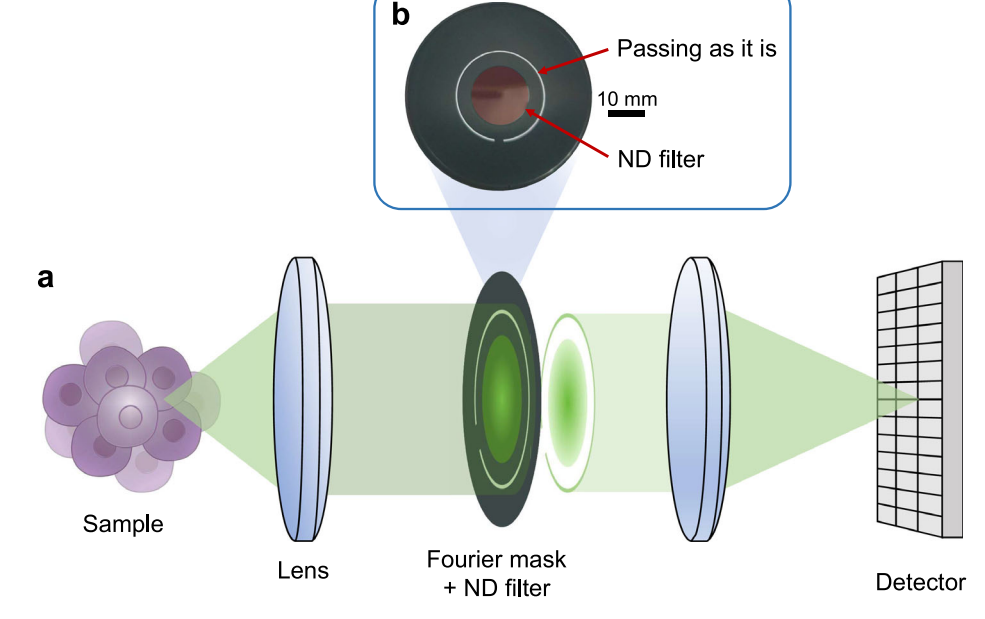
field evenly fills the pupil plane. However, in the case of samples not in the diffusive regime, the vicinity of the DC term of a Fourier field generally has a far stronger intensity than the support boundary, which makes the convergence of the HIO algorithm unstable; in this case, the support boundary is not well defined. This issue can be ascertained intuitively or empirically. If the intensity of the part far from the boundary is very strong, the intensity near the boundary will be seen as almost zero, making it difficult to satisfy the 'compact support' condition 44-46. Figure S2 exhibits how the intensity of the region far from the support boundary affects the reconstruction fidelity. The reconstruction fidelity decreases as the vicinity of the DC term becomes more dominant.

In particular, samples of major interest in biological and medical study, including cells and thin pathological tissue, have a dominant DC term. This means that the previous configuration of RDI cannot be utilized for such samples<sup>38</sup>. To resolve this issue, we modulated the Fourier spectrum by setting an ND filter and an obstruction with a Fourier mask at the Fourier plane to attenuate the intensity of the DC term of the Fourier field. The proposed method was simply implemented in a conventional microscope setup without a reference arm, as shown in Fig. 1a. The only difference with a conventional microscope was that RDI requires locating a Fourier mask at the pupil plane. An ND filter is attached to the Fourier mask to attenuate the low-frequency components (Fig. 1b). This Fourier field modulation via the Fourier mask and an ND filter is described with a formula and the specific values of the numerical aperture (Fig. S3). Additional implementation details, including the mask layout and the optical setup, are presented in the Methods and Fig. S4.

In this study, the amplitude attenuation was set to 1% (1/100), a value determined through simulations considering noise effects (see Fig. S5). This choice reflects a trade-off between suppressing the dominant DC term and maintaining robustness under low signal-to-noise ratio (SNR) conditions. While weaker attenuation (e.g., 1/10) resulted in lower overall reconstruction fidelity, stronger attenuation (e.g., 1/1000) yielded higher fidelity in noiseless cases but greatly reduced robustness as noise increased. The selected 1/100 condition provided the best balance between fidelity and noise tolerance.

The mask was fabricated by cutting aluminum, offering a simple and low-cost solution. However, this method limits the ability to produce fine or thin features. Lithographic fabrication enables higher precision but at a higher cost. While spatial light modulators offer flexibility for dynamic mask shaping, they are costly and introduce bulk, potentially offsetting the compactness and simplicity of the proposed system.

Fig. 1 | Schematics of reciprocal diffractive imaging for general samples. a The scattered field from a sample is transferred to a detector by relay lenses. The combination of the Fourier mask and an ND filter modulates the light in the Fourier plane. b Photograph of the Fourier mask and the ND filter. The low spatial frequency components in the Fourier spectrum are attenuated by the ND filter, and the light passes through the outermost ring shape. Created with BioRender.com.



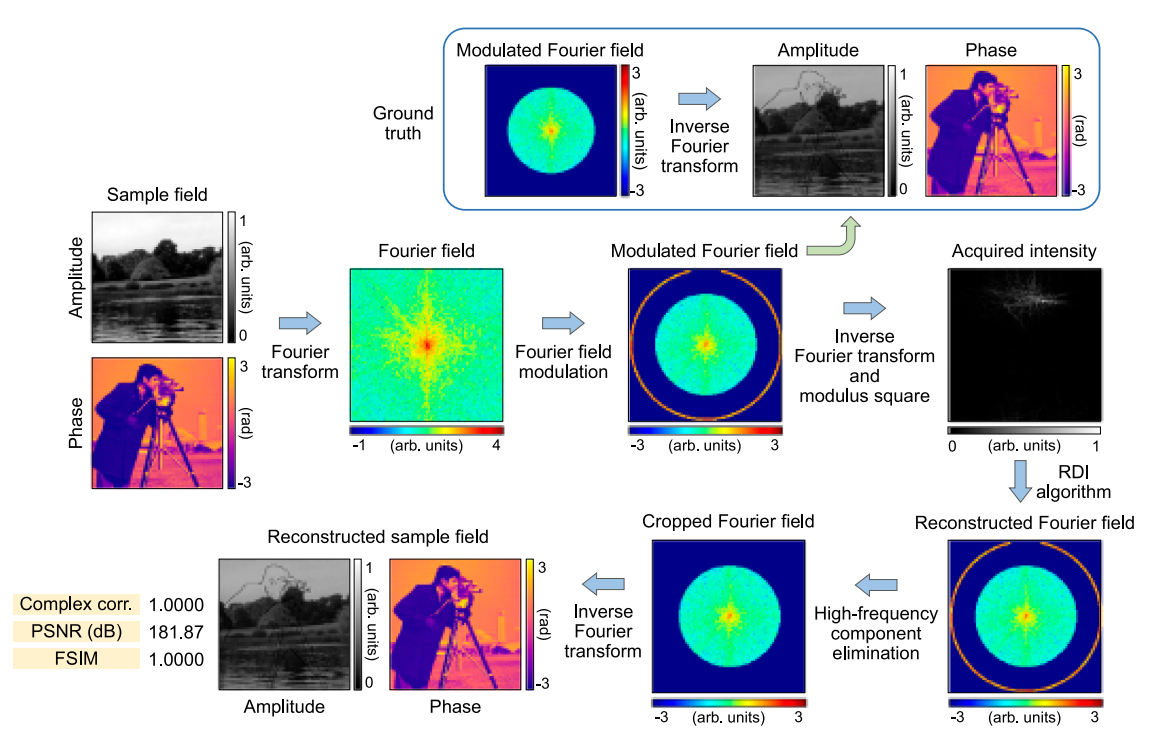


**Fig. 2** | **Principle of reciprocal diffractive imaging for general samples.** A schematic overview of the RDI process. The two-dimensional Fourier transform of a complex sample field—comprising both amplitude and phase—is spatially modulated at the pupil plane using a designed Fourier mask. The intensity image acquired at the detector corresponds to the inverse Fourier transform of the modulated spectrum. The RDI algorithm, based on the iterative hybrid input–output (HIO)

method, reconstructs the Fourier field from this intensity data. By isolating the outermost ring-shaped region of the reconstructed spectrum and applying an inverse Fourier transform, a band-limited estimate of the sample field is obtained. The reconstructed field is quantitatively compared with the ground truth using three fidelity metrics.

In addition to diminishing the low spatial frequency components of the Fourier spectrum using an ND filter, criteria for the design of the Fourier mask should be considered: maximizing the reconstruction fidelity while minimizing signal loss. The stronger the strength of the boundary part of the support compared with the interior, the higher the reconstruction fidelity. However, due to the loss of light and vulnerability to noise, the intensity of the low frequencies cannot be lowered indefinitely. To address this issue, we found that cropping near the boundary increases the reconstruction fidelity. Also, it was confirmed through simulation that as the outermost ring part is thinner, the reconstruction fidelity increases. The simulation results depending on the cropping area and the outermost ring part are shown in Figs. S6 and S7. It is presumed that this is because the boundary becomes more dominant compared to the ambient areas. Finally, noncentrosymmetry was ensured by cropping a portion of the support edge. The shape of the used mask was determined as in Fig. 1b. These design criteria are elucidated in Fig. S8.

Figure 1b describes the reconstruction process of the proposed RDI method based on the HIO algorithm. The algorithm reconstructs the sample field using the measured intensity and the information in the Fourier space. This algorithm is a reciprocal version of the HIO algorithm. The sample field to be reconstructed is s(x,y). S(u,v) denotes its two-dimensional (2D) Fourier transform. The sample field is Fourier-transformed and restricted to the shape of the Fourier filter. The intensity of the low-frequency components is greatly reduced according to the ND filter specifications, and only the boundary portion allows light to pass through as it is. The obstruction between the attenuated components and the support boundary helps the algorithm to converge. The modulated Fourier field is denoted by S'(u,v). The intensity of the inverse transform of S'(u,v) gives a constraint in image space:

$$|s'(x,y)| \equiv |\mathcal{F}^{-1}[S'(u,v)]|,$$
 (1)

where  $\mathcal{F}^{-1}$  denotes the 2D inverse Fourier transform. Using the constraints of the Fourier support and |s'(x,y)| in both Fourier and image spaces, S'(u,v) is retrieved iteratively. The 2D inverse Fourier transform of S'(u,v) is the bandlimited sample field. A detailed description of the HIO algorithm can be found elsewhere<sup>38,39</sup>. The feedback parameter in the HIO algorithm was set to 0.6, and the iteration process was run up to 1000 steps. To enhance robustness under noisy conditions, we employed a noise-robust version of the HIO algorithm<sup>47</sup>. This approach addresses convergence issues caused by inconsistencies between image and Fourier domain constraints. The relaxation parameter was set to 0.005 for the first 500 iterations and increased to 0.1 thereafter to accelerate convergence.

In simulation, the reconstructed field shows a correlation of 1.0000 with the ground truth, as shown in (Fig. 2a). Note that the ground truth means the numerical aperture-limited sample field. The generality of the proposed RDI method can be seen by the reconstruction results of various objects in Fig. S9, confirming its robustness across various imaging scenarios. The reconstruction fidelity depending on the iteration number and the collapsed time depending on the number of reconstructed pixels are described in Fig. S10. In the absence of noise, the reconstructed result reached a correlation of 0.99999 with the ground truth by the 181st iteration. Using a GPU (GeForce RTX 4090, NVIDIA Corp.), the reconstruction time for a 100,000-pixel image was under 5 s.

# **Experimental validation**

To validate the proposed RDI method, we first imaged well-characterized reference samples: a United States Air Force (USAF) resolution target and spherical microbeads as an amplitude object and a phase object, respectively. The measured intensity images exhibited non-uniform distributions, with high-frequency components near the support boundary appearing greatly stronger than those in the central region—an expected outcome of the Fourier-plane modulation.

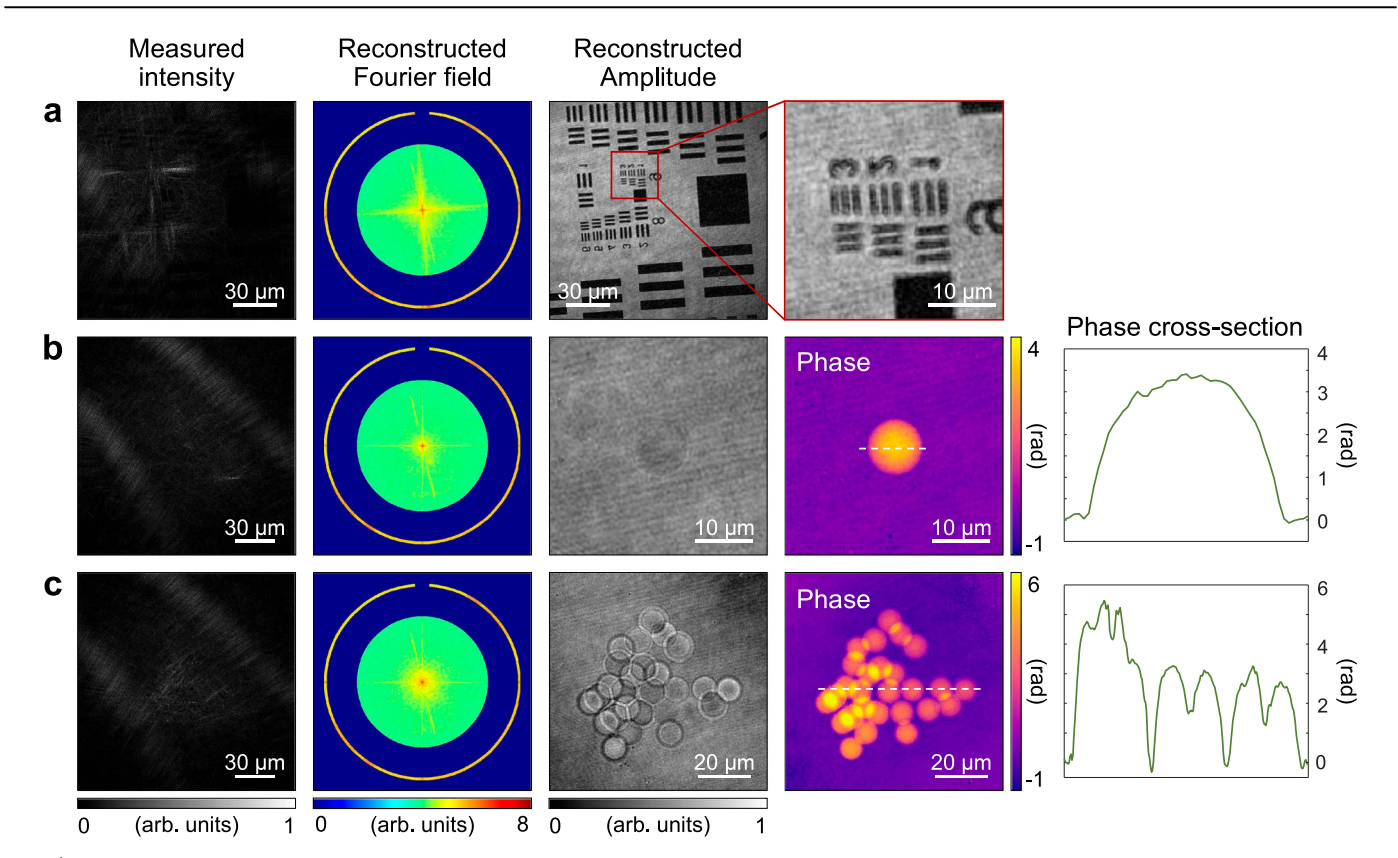


**Fig. 3** | **Experimental validation using known samples.** The sample fields were retrieved by the RDI algorithm: a United States Air Force resolution target (a), spherical polystyrene microbead (b), and microbead cluster (c). The measured intensities, retrieved Fourier fields, retrieved amplitudes, and retrieved phases are

shown. The cross-section plots of the phase images are provided along the white dotted lines in **(b)** and **(c)**. The phase unwrapping algorithm was applied. The Fourier spectrum is represented on a log scale.

The reconstructed amplitude image of the USAF target showed the expected sample structure (Fig. 3a). The smallest pattern of the USAF target (Group 9, Element 3) has  $0.78\,\mu m$  spacing and was well resolved by the imaging system whose theoretical resolution is  $0.46\,\mu m$ . The reconstructed phase image of a microbead shows its expected spherical shapes (Fig. 3b). The phase delay at the bead center was  $3.41\, rad$ , and this value is comparable to the results from the off-axis holography setup in ref. 35. Furthermore, a more complex configuration comprising multiple clustered beads was successfully imaged, demonstrating the method's robustness across varying sample geometries (Fig. 3c). Cross-section plots of the phase images provide a more quantitative view of the sample's phase distribution. The observed background unevenness is likely due to static aberrations from the lenses or the ND filter. These artifacts can be mitigated using a background subtraction method.

## **Biological application**

To demonstrate the applicability of the proposed RDI method to real-world biological specimens, we imaged animal tissues (BCN482, US Biolab Corp.) to demonstrate the applicability of the proposed method. Three types of tissue were successfully reconstructed, as shown in (Fig. 4a). Because these tissues were stained, they also showed contrast in the amplitude images. Both the reconstructed amplitude and phase maps exhibited high contrast and resolution, revealing the appearance of discernible microscopic structures. Because phase unwrapping was broken due to high phase delay in the granule structures, we presented these phase distributions without unwrapping and with a cyclic color map.

Biological cells were also employed in the quantitative microscope. Living biological cells COS7 and Hs68 were imaged, and the reconstructed phase distribution showed the morphology and characteristics of the cells as it is (Fig. 5a, b). In addition, a strong point of the RDI method is that this technique only requires a single-shot intensity image, making it an excellent

candidate for the imaging of dynamic samples <sup>18,49</sup>. To highlight this capability, we imaged motile NIH3T3 cells and captured their temporal evolution at a frame rate of 4.25 fps (Fig. 5c). The temporal resolution is limited only by the camera's frame rate and can exceed 4.25 fps in faster imaging setups. The cross-section plot of the NIH3T3 cell highlights the internal structural heterogeneity of the sample.

Notably, the original RDI configuration was unable to reconstruct these same samples, including the microbead cluster (Fig. 3c) and moving cells (Fig. 5c), due to its sensitivity to dominant low-frequency components. This performance gap is illustrated in Supplementary Fig. S11, underscoring the effectiveness of the proposed generalized RDI approach.

### **Discussion**

We proposed RDI for microscopy to retrieve the quantitative phase of various samples. The design of the Fourier mask and the attenuation of the ND filter effectively modulated the transmitted field at the pupil plane of the microscope, enabling the RDI algorithm to work for samples with a strong DC term. The fidelity of the proposed method was demonstrated via objects with known structures. Imaging of biological tissues and cells revealed the promising capability of the proposed method for biological studies.

The RDI method reconstructs complex sample fields from a single-shot intensity measurement in a non-interferometric manner without requiring special optics or a spatial light modulator. In addition, this method does not require oversampling beyond the Nyquist sampling rate, fully utilizing the space-bandwidth product of the imaging system. Although each imaging method has its own advantages, it is interesting to compare the proposed method with the recently developed non-interferometric KK holographic imaging as it has similar advantages. The RDI method only requires a single-shot intensity image and does not exploit an illumination unit. More importantly, the presented method has a significant advantage over KK holography: the reconstruction fidelity is kept as the phase of a

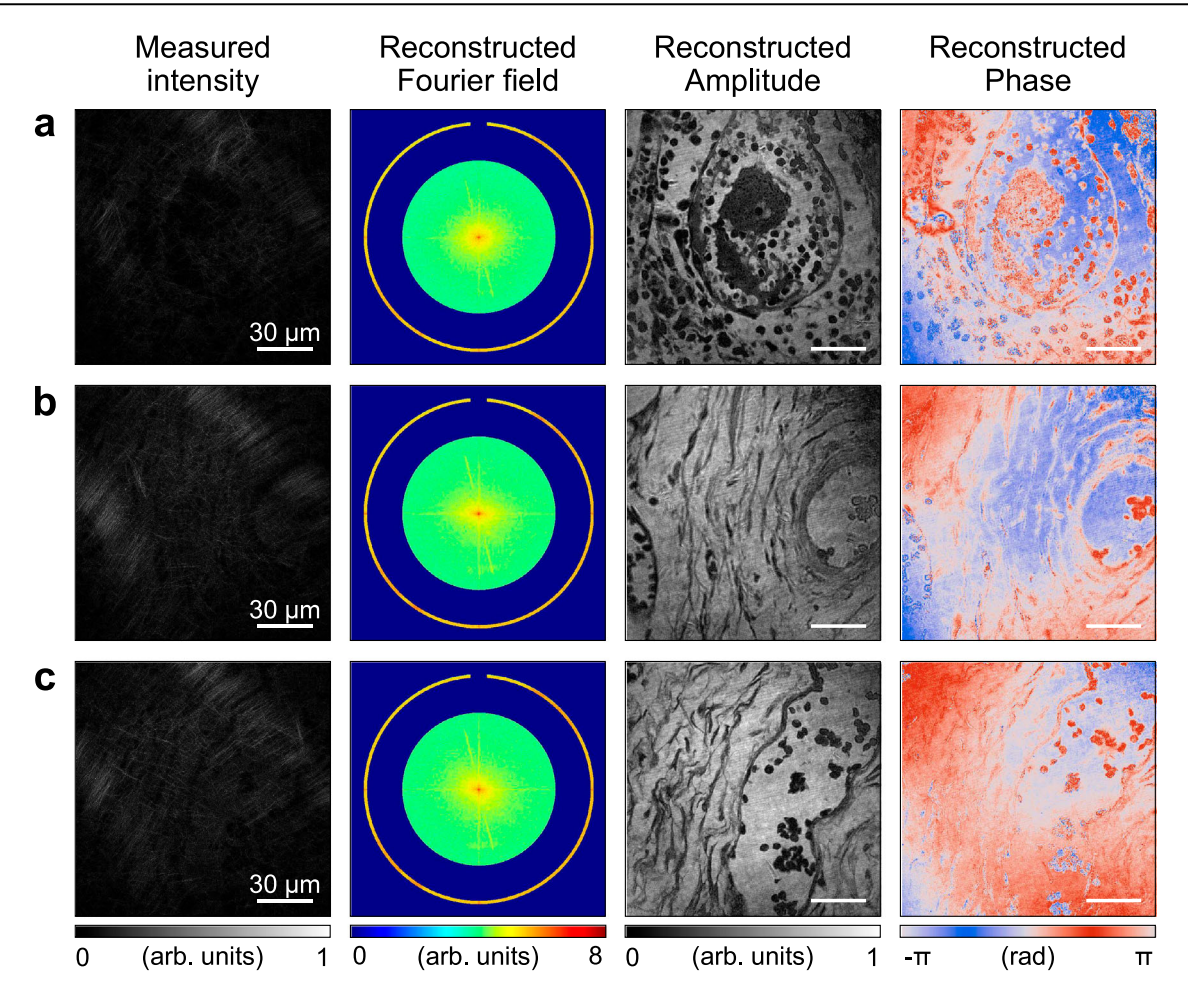


Fig. 4 | Results for biological tissue imaging. The sample fields scattered from biological tissues were retrieved by the RDI algorithm: lymph node (a), adjacent normal ovary (b), and adjacent normal prostate (c) tissues. The measured intensities,

retrieved Fourier fields, retrieved amplitudes, and retrieved phases are shown. The Fourier spectrum is represented on a log scale.

sample field increases (Fig. S12). Moreover, RDI is applicable to general samples without relying on weak scattering or thin-sample assumptions, unlike DPC microscopy or Fourier ptychography.

Despite its advantages, the proposed method has several limitations that warrant further investigation. The ND filter attenuates not only the DC term but also other frequency components, which may reduce reconstruction fidelity in low-SNR conditions—especially for weak spectral components (Fig. S5). This limitation could potentially be mitigated by employing an apodizing or custom-designed ND filter that selectively attenuates low-frequency components while preserving critical information content. Another limitation is the reduced effective NA caused by Fourier-space cropping from the mask geometry (Fig. S3), which may lower the achievable space-bandwidth product. Nevertheless, the proposed method remains data-efficient compared to iterative techniques like FPM, which require redundant intensity measurements.

Although our implementation relies only on a simple aluminum mask and a commercially available ND filter—highlighting the method's experimental simplicity—further optimization of the mask design could improve NA utilization without compromising support constraints. In particular, a Fisher information matrix—based optimization framework may be employed to systematically tune the mask parameters under varying imaging conditions and noise levels<sup>51,52</sup>.

In addition, integration with recent advances in Fourier spectrum modulation techniques may further enhance the performance of RDI in optical microscopy. While the proposed method allows rapid acquisition of dynamic samples, real-time visualization is limited by the iterative nature of the reconstruction process (Fig. S10). This is a potential drawback compared

to methods like TIE, KK holography, and DPC microscopy, which support near real-time reconstruction. To address this, future developments could draw inspiration from phase retrieval approaches that incorporate Fourier modulation strategies and artificial intelligence–based reconstruction frameworks, such as machine learning<sup>53–55</sup>. Furthermore, adopting variants of gradient descent–based algorithms may help reduce computational load by decreasing both reconstruction time and the number of required iterations, while also improving robustness under noisy conditions<sup>56–58</sup>. These directions collectively point toward the potential for real-time, high-fidelity, and noise-resilient RDI implementations.

Process errors in mask fabrication can influence reconstruction fidelity. To assess this, we simulated variations in mask radius under an SNR of 50 (Fig. S13). Even with a 15% deviation, the decrease in reconstruction fidelity (complex correlation) was less than 0.5%. As actual fabrication errors are expected to be within 10%, the impact is minimal. However, other forms of deviation may also affect performance, and further investigation is warranted.

Owing to its non-interferometric nature, the proposed method can be readily integrated into optical systems employing spatially coherent broadband light sources, such as superluminescent diodes. Additionally, the use of temporally incoherent illumination may further suppress coherent noise, thereby enhancing performance in applications such as nanoparticle detection. Beyond two-dimensional imaging, the RDI framework can be extended to holotomography or three-dimensional QPI<sup>59</sup> by incorporating beam-sweeping modules—such as LED arrays<sup>31,60</sup> or digital micromirror devices<sup>61,62</sup>—to modulate the illumination wavefront. In such cases, the DC component shifts according to the spatial frequency associated with each

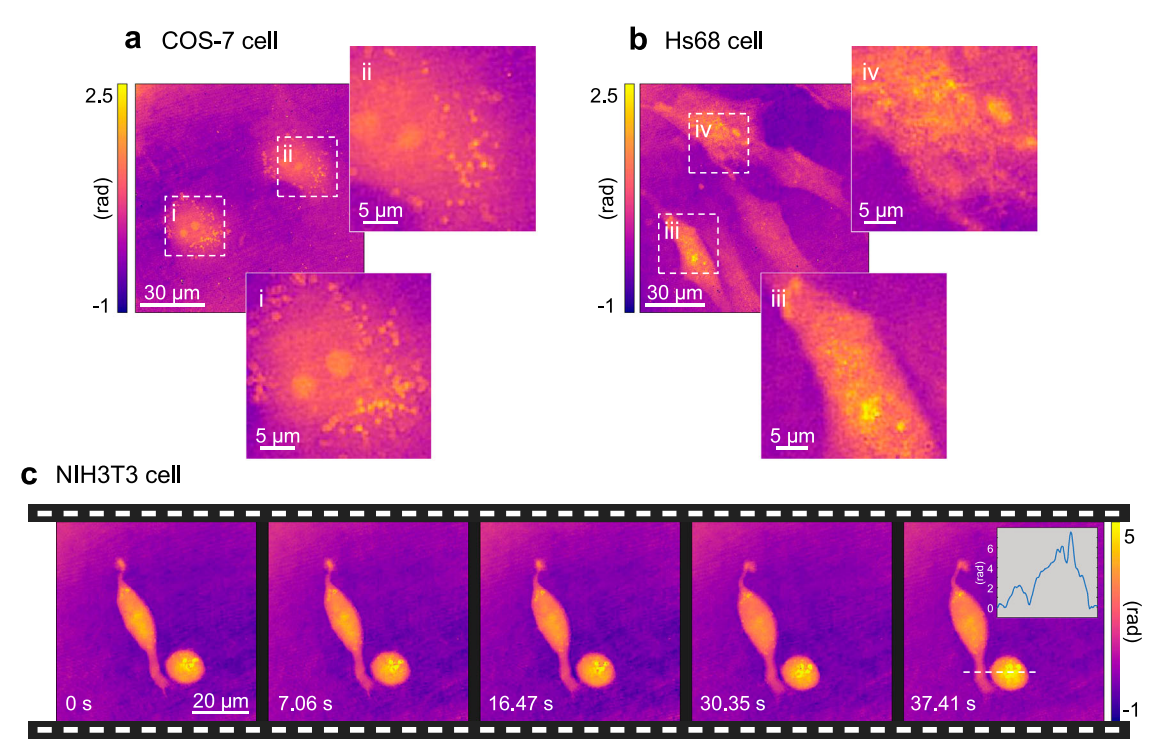


Fig. 5 | Static and dynamic quantitative phase imaging of biological cells. The reconstructed phase distributions of biological cells COS7 (a) and Hs68 (b). The dotted-line boxes "i–iv" are enlarged to inset for visualization.  $\bf c$  Several frames for

the quantitative phase map over time of moving NIH3T3 cells. A cross-section plot along the white dotted line is included as an inset. The phase unwrapping algorithm was applied.

incident angle, forming a ring-shaped distribution in the Fourier plane. This configuration allows for the use of annular ND filters optimized for angle-dependent suppression of low-frequency components.

The reference-free and compact nature of our microscope makes it well-suited for integration with other modalities, enabling multimodal imaging applications such as molecular vibrational imaging <sup>63</sup> and fluorescence microscopy<sup>64</sup>. For thick, heterogeneous samples like whole organs, the proposed method could be combined with complementary techniques that correct for sample-induced artifacts<sup>65–67</sup>. Given these extensions, we anticipate that the RDI method will find broad utility not only in biological imaging <sup>15,68,69</sup> but also in other holography-driven fields, including precision metrology and industrial inspection<sup>70,71</sup>.

# Methods

# **Experimental setup**

The detailed experimental setup is depicted in Fig. S4. The light source used is a coherent diode-pumped solid-state laser with a wavelength of 531.65 nm (Laserglow Technologies, S533001FX). A collimated plane wave illuminates a sample after passing through a tube lens (L1) and a condenser lens (OL1, Olympus Inc., LMPLFLN50X). The light scattered from the sample is collected by an objective lens (OL2, Olympus Inc., UPLSAPO60XW). Then, the light in order passes through relay lenses (L2, L3) and is modulated in the Fourier plane by the custom-made aluminum mask (Fourier mask) and an ND filter (Edmund Optics Inc., 54-459). The modulated light is transferred to a camera (XIMEA, MQ042MG-CM) by a lens (L4). A linear polarizer (Thorlabs LPVISE100-A) is placed immediately before the camera to enhance contrast; however, it is not essential for the operation of the method. The camera records the intensity distribution of the transmitted light. Using this intensity image and the known design of the Fourier mask, the RDI algorithm reconstructs the complex optical field scattered by the sample.

#### Preparation of biological cells

COS7(ATCC, CRL-1651), Hs68 (ATCC, CRL-1635), and NIH3T3(ATCC, CRL-1658) cells were maintained in Dulbecco's modified Eagle's Medium

(DMEM; ATCC, 30-2002) supplemented with 10% fetal bovine serum (Thermo FisherScientific Inc.) and 1% (v/v) penicillin/streptomycin (Thermo Fisher Scientific Inc.) at 37 °C in a 5% CO<sub>2</sub> incubator. For imaging experiments, cells were seeded into specialized glass-bottom imaging dishes (TomoDish, Tomocube Inc.) with a coverslip thickness of #1.5H and an 80  $\mu$ m gap designed specifically for high-resolution microscopy, at a density of  $\sim 1 \times 10^5$  cells/mL. Imaging was performed directly on live cells without further fixation or staining.

### Preparation of biological tissues

Animal tissues (BCN482, US Biolab Corp.) were formalin-fixed and paraffin-embedded (FFPE). Specifically, tissues were fixed in 10% neutral-buffered formalin (NBF) within 30 min post excision, embedded in immunohistochemistry (IHC)-grade paraffin, and sectioned at ~5  $\mu m$  thickness using standard histological methods. Sections were then mounted onto standard microscope glass slides using an aqueous mounting medium (e.g., Fluoromount-G; refractive index n=1.37-1.38). Prior to imaging, the samples were sealed to prevent drying and minimize optical artifacts.

## Data availability

The sample data for the implementation of the RDI method are available at our GitHub repository: github.com/BMOLKAIST/RDI-for-Microscopy-2024.

#### Code availability

The MATLAB codes for the implementation of the RDI method are available at our GitHub repository: github.com/BMOLKAIST/RDI-for-Microscopy-2024.

Received: 11 May 2025; Accepted: 22 August 2025; Published online: 29 September 2025

#### References

1. Gabor, D. A new microscopic principle. *Nature* **161**, 777–778 (1948).

- Park, Y., Depeursinge, C. & Popescu, G. Quantitative phase imaging in biomedicine. *Nat. Photonics* 12. 578–589 (2018).
- Bokemeyer, A. et al. Quantitative phase imaging using digital holographic microscopy to assess the degree of intestinal inflammation in patients with ulcerative colitis. *J. Clin. Med.* 12, 4067 (2023).
- van der Horst, J., Trull, A. K. & Kalkman, J. Deep-tissue label-free quantitative optical tomography. Optica 7, 1682–1689 (2020).
- Park, J. et al. Quantification of structural heterogeneity in H&E stained clear cell renal cell carcinoma using refractive index tomography. Biomed. Opt. Express 14, 1071–1081 (2023).
- Liu, Y. & Xu, J. High-resolution microscopy for imaging cancer pathobiology. Curr. Pathobiol. Rep. 7, 85–96 (2019).
- Oh, J. et al. Three-dimensional label-free observation of individual bacteria upon antibiotic treatment using optical diffraction tomography. *Biomed. Opt. Express* 11, 1257–1267 (2020).
- Choi, S. Y., Oh, J., Jung, J., Park, Y. & Lee, S. Y. Three-dimensional label-free visualization and quantification of polyhydroxyalkanoates in individual bacterial cell in its native state. *Proc. Natl Acad. Sci.* 118, e2103956118 (2021).
- Kim, G. et al. Rapid species identification of pathogenic bacteria from a minute quantity exploiting three-dimensional quantitative phase imaging and artificial neural network. Light. Sci. Appl. 11, 190 (2022).
- Memmolo, P., Miccio, L., Merola, F., Mugnano, M. & Ferraro, P. Hydrodynamic red blood cells deformation by quantitative phase microscopy and Zernike polynomials. Front. Phys. 7, 111 (2019).
- Shu, X. et al. Artificial-intelligence-enabled reagent-free imaging hematology analyzer. Adv. Intell. Syst. 3, 2000277 (2021).
- Ong, J. J. et al. Optical diffraction tomography and image reconstruction to measure host cell alterations caused by divergent Plasmodium species. Spectrochim Acta Part A Mol. Biomol. Spectrosc. 286, 122026 (2023).
- Kim, G., Jo, Y., Cho, H., Min, H. -s. & Park, Y. Learning-based screening of hematologic disorders using quantitative phase imaging of individual red blood cells. *Biosens. Bioelectron.* 123, 69–76 (2019).
- Lee, S. Y., Park, H. J., Best-Popescu, C., Jang, S. & Park, Y. K. The effects of ethanol on the morphological and biochemical properties of individual human red blood cells. *PLoS ONE* 10, e0145327 (2015).
- Esposito, M. et al. TGF-β-induced DACT1 biomolecular condensates repress Wnt signalling to promote bone metastasis. *Nat. Cell Biol.* 23, 257–267 (2021).
- Lee, S.-A. et al. OASL phase condensation induces amyloid-like fibrillation of RIPK3 to promote virus-induced necroptosis. *Nat. Cell Biol.* 25, 92–107 (2023).
- Cho, M. J., Kim, C.-E., Shin, Y. H., Kim, J. K. & Pack, C.-G. Influence of chemical and genetic manipulations on cellular organelles quantified by label-free optical diffraction tomography. *Anal. Chem.* 95, 13478–13487 (2023).
- Park, S. et al. Label-free tomographic imaging of lipid droplets in foam cells for machine-learning-assisted therapeutic evaluation of targeted nanodrugs. ACS Nano 14, 1856–1865 (2020).
- Steike, D. R. et al. Digital holographic microscopy for label-free detection of leukocyte alternations associated with perioperative inflammation after cardiac surgery. Cells 11, 755 (2022).
- Bianco, V. et al. Classifying breast cancer and fibroadenoma tissue biopsies from paraffined stain-free slides by fractal biomarkers in Fourier Ptychographic Microscopy. *Comput. Struct. Biotechnol. J.* 24, 225–236 (2024).
- Xin, L. et al. Label-free assessment of the drug resistance of epithelial ovarian cancer cells in a microfluidic holographic flow cytometer boosted through machine learning. ACS Omega 6, 31046–31057 (2021).
- 22. Koo, S. -e., Jang, S., Park, C. J., Cho, Y.-U. & Park, Y. Unique red blood cell morphology detected in a patient with myelodysplastic

- syndrome by three-dimensional refractive index tomography. *Lab. Med. Online* **9**, 185–188 (2019).
- 23. Wang, P., Bista, R., Bhargava, R., Brand, R. E. & Liu, Y. Spatial-domain low-coherence quantitative phase microscopy for cancer diagnosis. *Opt. Lett.* **35**, 2840–2842 (2010).
- 24. Postnov, D. D., Tang, J., Erdener, S. E., Kılıç, K. & Boas, D. A. Dynamic light scattering imaging. *Sci. Adv.* **6**, eabc4628 (2020).
- Shechtman, Y. et al. Phase retrieval with application to optical imaging: a contemporary overview. *IEEE Signal Process. Mag.* 32, 87–109 (2015).
- 26. Lassègues, P. et al. Field and intensity correlations: the Siegert relation from stars to quantum emitters. *Eur. Phys. J. D* **76**, 246 (2022).
- Gureyev, T., Roberts, A. & Nugent, K. Partially coherent fields, the transport-of-intensity equation, and phase uniqueness. *JOSA A* 12, 1942–1946 (1995).
- 28. Zuo, C. et al. High-resolution transport-of-intensity quantitative phase microscopy with annular illumination. *Sci. Rep.* **7**, 7654 (2017).
- Hamilton, D. & Sheppard, C. Differential phase contrast in scanning optical microscopy. J. Microsc. 133, 27–39 (1984).
- Tian, L. & Waller, L. Quantitative differential phase contrast imaging in an LED array microscope. Opt. Express 23, 11394–11403 (2015).
- 31. Zheng, G., Horstmeyer, R. & Yang, C. Wide-field, high-resolution Fourier ptychographic microscopy. *Nat. Photonics* **7**, 739–745 (2013).
- 32. Zheng, G., Shen, C., Jiang, S., Song, P. & Yang, C. Concept, implementations and applications of Fourier ptychography. *Nat. Rev. Phys.* **3**, 207–223 (2021).
- Baek, Y. & Park, Y. Intensity-based holographic imaging via spacedomain Kramers–Kronig relations. *Nat. Photonics*, 15, 354–360 (2021).
- Pavillon, N., Seelamantula, C. S., Kühn, J., Unser, M. & Depeursinge,
  C. Suppression of the zero-order term in off-axis digital holography
  through nonlinear filtering. *Appl. Opt.* 48, H186–H195 (2009).
- 35. Oh, J., Hugonnet, H. & Park, Y. Quantitative phase imaging via the holomorphic property of complex optical fields. *Phys. Rev. Res.* **5**, L022014 (2023).
- Shen, C., Liang, M., Pan, A. & Yang, C. Non-iterative complex wavefield reconstruction based on Kramers–Kronig relations. *Photonics Res.* 9, 1003–1012 (2021).
- Zuo, C. et al. Transport of intensity equation: a tutorial. Opt. Lasers Eng. 135, 106187 (2020).
- Oh, J., Hugonnet, H. & Park, Y. Non-interferometric stand-alone single-shot holographic camera using reciprocal diffractive imaging. *Nat. Commun.* 14, 4870 (2023).
- Fienup, J. R. Reconstruction of a complex-valued object from the modulus of its Fourier transform using a support constraint. *JOSA A* 4, 118–123 (1987).
- 40. Williams, G. et al. Fresnel coherent diffractive imaging. *Phys. Rev. Lett.* **97**, 025506 (2006).
- 41. Williams, G. J., Quiney, H. M., Peele, A. G. & Nugent, K. A. Coherent diffractive imaging and partial coherence. *Phys. Rev. B* **75**, 104102 (2007).
- 42. Lo, Y. H. et al. In situ coherent diffractive imaging. *Nat. Commun.* 9, 1826 (2018).
- Kang, J., Takazawa, S., Ishiguro, N. & Takahashi, Y. Single-frame coherent diffraction imaging of extended objects using triangular aperture. *Opt. Express* 29, 1441–1453 (2021).
- Rosenblatt, J. Phase retrieval. Commun. Math. Phys. 95, 317–343 (1984).
- 45. Tradonsky, C. et al. Rapid laser solver for the phase retrieval problem. *Sci. Adv.* **5**, eaax4530 (2019).
- Millane, R. Multidimensional phase problems. JOSA A 13, 725–734 (1996).
- Trahan, R. & Hyland, D. Mitigating the effect of noise in the hybrid input–output method of phase retrieval. *Appl. Opt.* 52, 3031–3037 (2013).

- 48. Picazo-Bueno, J. Á. et al. Single capture bright field and off-axis digital holographic microscopy. *Opt. Lett.* **48**, 876–879 (2023).
- Khmaladze, A. et al. Cell volume changes during apoptosis monitored in real time using digital holographic microscopy. *J. Struct. Biol.* 178, 270–278 (2012).
- Oh, J., Lee, K. & Park, Y. Single-shot reference-free holographic imaging using a liquid crystal geometric phase diffuser. *Laser Photonics Rev.* 16, 2100559 (2022).
- Fournier, C., Denis, L. & Fournel, T. On the single point resolution of on-axis digital holography. J. Opt. Soc. Am. A 27, 1856–1862 (2010).
- Chao, J., Sally Ward, E. & Ober, R. J. Fisher information theory for parameter estimation in single molecule microscopy: tutorial. *J. Opt. Soc. Am. A* 33, B36–B57 (2016).
- Wang, K. et al. On the use of deep learning for phase recovery. Light. Sci. Appl. 13, 4 (2024).
- Hao, J. et al. Lensless phase retrieval based on deep learning used in holographic data storage. Opt. Lett. 46, 4168–4171 (2021).
- Li, R., Pedrini, G., Huang, Z., Reichelt, S. & Cao, L. Physics-enhanced neural network for phase retrieval from two diffraction patterns. *Opt. Express* 30, 32680–32692 (2022).
- 56. Chang, X., Bian, L. & Zhang, J. Large-scale phase retrieval. *eLight* 1, 1–12 (2021).
- Mignacco, F., Urbani, P. & Zdeborová, L. Stochasticity helps to navigate rough landscapes: comparing gradient-descent-based algorithms in the phase retrieval problem. *Mach. Learn. Sci. Technol.* 2, 035029 (2021).
- Ji, L. & Tie, Z. Proc. 2016 IEEE 13th International Conference on Signal Processing (ICSP). 320–325 (IEEE, 2016). https://ieeexplore.ieee.org/ document/7877848.
- 59. Kim, G. et al. Holotomography. Nat. Rev. Methods Prim. 4, 51 (2024).
- Li, J. et al. High-speed in vitro intensity diffraction tomography. Adv. Photonics 1, 066004–066004 (2019).
- Hugonnet, H., Lee, M. & Park, Y. Optimizing illumination in threedimensional deconvolution microscopy for accurate refractive index tomography. Opt. Express 29, 6293–6301 (2021).
- Shin, S. et al. in *Quantitative Phase Imaging II*. 156–163 (SPIE, 2016). https://doi.org/10.1117/12.2216769.
- Tamamitsu, M. et al. Label-free biochemical quantitative phase imaging with mid-infrared photothermal effect. Optica 7, 359–366 (2020).
- Butola, A. et al. Multimodal on-chip nanoscopy and quantitative phase imaging reveals the nanoscale morphology of liver sinusoidal endothelial cells. *Proc. Natl Acad. Sci.* 118, e2115323118 (2021).
- Schwertner, M., Booth, M. J. & Wilson, T. Characterizing specimen induced aberrations for high NA adaptive optical microscopy. *Opt. Express* 12, 6540–6552 (2004).
- Chen, M., Ren, D., Liu, H.-Y., Chowdhury, S. & Waller, L. Multi-layer Born multiple-scattering model for 3D phase microscopy. *Optica* 7, 394–403 (2020).
- 67. Lee, M., Hugonnet, H. & Park, Y. Inverse problem solver for multiple light scattering using modified Born series. *Optica* **9**, 177–182 (2022).
- Dunn, K. J. et al. Optical diffraction tomography for assessing single cell models in angular light scattering. *Biomed. Opt. Express* 15, 973–990 (2024).
- Khmaladze, A. et al. Dual-wavelength linear regression phase unwrapping in three-dimensional microscopic images of cancer cells. Opt. Lett. 36, 912–914 (2011).

- 70. Jung, J. et al. Multi spectral holographic ellipsometry for a complex 3D nanostructure. *Opt. Express* **30**, 46956–46971 (2022).
- 71. Kim, K., Yoon, J. & Park, Y. Large-scale optical diffraction tomography for inspection of optical plastic lenses. *Opt. Lett.* **41**, 934–937 (2016).

### **Acknowledgements**

This work was supported by National Research Foundation of Korea grant funded by the Korea government (MSIT) (RS-2024-00442348, RS-2024-00440577, 2022M3H4A1A02074314), Korea Institute for Advancement of Technology (KIAT) through the International Cooperative R&D program (P0028463), the Commercialization Promotion Agency for R&D Outcomes (COMPA) funded by MSIT (2710068936), and the Samsung Research Funding Center of Samsung Electronics under Grant SRFC-IT1401-08.

### **Author contributions**

J.O. and Y.P. conceived the project. J.O. designed the optical system, conducted the experiment, and analyzed the data. H.H. provided a discussion of the experimental results. W.P. prepared biological samples. All authors wrote the manuscript. Y.P. provided supervision.

## **Competing interests**

The authors declare no competing interests.

## **Additional information**

**Supplementary information** The online version contains supplementary material available at https://doi.org/10.1038/s42005-025-02292-x.

**Correspondence** and requests for materials should be addressed to YongKeun Park.

**Peer review information** Communications Physics thanks Dan Dan and the other, anonymous, reviewer(s) for their contribution to the peer review of this work. A peer review file is available.

Reprints and permissions information is available at http://www.nature.com/reprints

**Publisher's note** Springer Nature remains neutral with regard to jurisdictional claims in published maps and institutional affiliations.

Open Access This article is licensed under a Creative Commons Attribution 4.0 International License, which permits use, sharing, adaptation, distribution and reproduction in any medium or format, as long as you give appropriate credit to the original author(s) and the source, provide a link to the Creative Commons licence, and indicate if changes were made. The images or other third party material in this article are included in the article's Creative Commons licence, unless indicated otherwise in a credit line to the material. If material is not included in the article's Creative Commons licence and your intended use is not permitted by statutory regulation or exceeds the permitted use, you will need to obtain permission directly from the copyright holder. To view a copy of this licence, visit http://creativecommons.org/licenses/by/4.0/.

© The Author(s) 2025